JACS
JOURNAL OF THE AMERICAN CHEMICAL SOCIETY
pubs.acs.org/JACS
Article

Red Light-Initiated Cross-Linking of NIR Probes to Cytoplasmic RNA: An Innovative Strategy for Prolonged Imaging and Unexpected Tumor Suppression

Shuyue Ye, Chaoxiang Cui, Xiaju Cheng, Meng Zhao, Qiulian Mao, Yuqi Zhang, Anna Wang, Jing Fang, Yan Zhao, and Haibin Shi*

Cite This: J. Am. Chem. Soc. 2020, 142, 21502−21512

Read Online

ACCESS | Metrics & More | Article Recommendations | Supporting Information

ABSTRACT: Improving the enrichment of drugs or theranostic agents within tumors is very vital to achieve effective cancer diagnosis and therapy while greatly reducing the dosage and damage to normal tissues. Herein, as a proof of concept, we for the first time report a red light-initiated probe-RNA cross-linking (RLIPRC) strategy that can not only robustly promote the accumulation and retention of the probe in the tumor for prolonged imaging but also significantly inhibits the tumor growth. A near-infrared (NIR) fluorescent probe *f*-CR consisting of a NIR dye (Cyanine 7) as a signal reporter, a cyclic-(arginine-glycine-aspartic acid) (cRGD) peptide for tumor targeting, and a singlet oxygen ($^1O_2$)-sensitive furan moiety for RNA cross-linking was rationally designed and synthesized. This probe possessed both passive and active tumor targeting abilities and emitted intense NIR/photoacoustic (PA) signals, allowing for specific and sensitive dual-modality imaging of tumors in vivo. Notably, probe *f*-CR could be specifically and covalently cross-linked to cytoplasmic RNAs via the cycloaddition reaction between furan and adenine, cytosine, or guanine under the oxidation of $^1O_2$ generated in situ by irradiation of methylene blue (MB) with 660 nm laser light, which effectively blocks the exocytosis of the probes resulting in enhanced tumor accumulation and retention. More excitingly, for the first time, we revealed that the covalent cross-linking of probe *f*-CR to cytoplasmic RNAs could induce severe apoptosis of cancer cells leading to remarkable tumor suppression. This study thus represents the first red light-initiated RNA cross-linking system with high potential to improve the diagnostic and therapeutic outcomes of tumors in vivo.

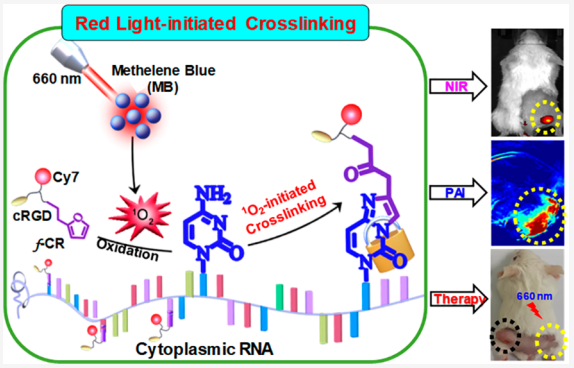

INTRODUCTION

As an important part of molecular imaging techniques, the molecular probe is becoming a fascinating tool for accurate cancer diagnosis and effective treatment.[1] To date, various types of molecular probes including small molecules,[2−5] macromolecules,[6−8] inorganic nanomaterials,[9,10] aptamers,[11,12] etc.[13−18] have been successfully developed for tumor imaging and therapeutic applications in living subjects.[19,20] Nevertheless, the limited accumulation of probes at targeted disease regions always causes unsatisfactory diagnostic and therapeutic outcomes.[21−27] To address this issue, a high dose of theranostic agents was usually administered[28] or utilizing bionanomaterials with long blood circulation, low renal clearance, and capillary leakage to improve their enrichment at the disease site,[29−32] which inevitably causes severe side effect to the body. Recently, stimuli-mediated self-assembly approaches have been reported to maximize the accumulation and retention of theranostic agents within tumors for improving the tumor diagnostic and therapeutic efficacy.[33−38] Many tumor microenvironment (TME)-responsive molecules that can be induced by certain stimuli such as cancer-associated enzymes,[39,40] acidic pH,[41] redox,[42] hypoxia,[43] etc.[44−49] to locally form aggregates or nanoparticles within tumors resulting in enhanced imaging signals and therapeutic efficacy were developed.[50−53] Despite the evident improvement achieved, the complicated biological environment may unavoidably pose unwanted particle aggregation and significant entrapment by the reticuloendothelial system (RES) leading to unsatisfactory theranostic outcomes.[54,55]

Light as a promising and controllable external stimulus has been widely applied in various biomedical applications due to its simplicity, low-cost, spatiotemporal addressability, and minimal invasiveness.[56] For example, the photo-cross-linking technique as an effective tool for covalent attachment of

Received: October 10, 2020
Published: December 11, 2020

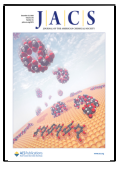

https://dx.doi.org/10.1021/jacs.0c10755
J. Am. Chem. Soc. 2020, 142, 21502−21512

Scheme 1. Red Light-Initiated Crosslinking of *f*-CR to Cytoplasmic RNAs for Prolonged Imaging and Suppression of Tumors

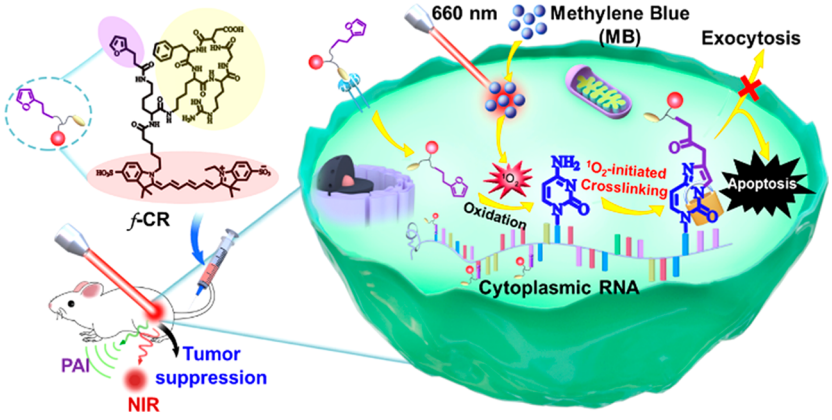

molecules onto their targets has been well-established for studying the intermolecular interaction of drug-targets,[57−59] protein−protein,[60] protein−DNA,[61,62] etc.[63] Unfortunately, the broad biological applications of this photo-cross-linking approach in living systems were impeded by the limited tissue penetration and potential phototoxicity of ultraviolet (UV) light.[64] Madder and co-workers[65] have recently developed a versatile red light-controlled cross-linking chemistry based on furan for studying a large variety of biomolecular interactions with spatiotemporal resolution, including DNA−DNA[66,67] and protein−RNA.[68,69] However, in vivo application of this cross-linking strategy has not been exploited yet. Ribonucleic acid (RNA) as a central conduit plays a pervasive and important role in cell information transmission and gene regulation.[70] A large number of studies have demonstrated that the modification of RNA structure can induce abnormal expression of downstream proteins leading to obvious cell apoptosis, which could potentially be used to treat cancer and other diseases.[71−75] Inspired by this, it is highly significant to employ this red light-mediated cross-linking approach to spatiotemporally manipulate the anchoring of theranostic agents onto RNAs in cancer cells for prolonged imaging and effective tumor therapy.

Herein, we for the first time report a novel red light-initiated probe-RNA cross-linking (RLIPRC) strategy for enhanced tumor imaging and effective tumor suppression. As depicted in Scheme 1, we rationally designed and synthesized a small molecule NIR probe *f*-CR that consists of a NIR dye (Cy7) as a signal reporter, a cRGD peptide that can specifically bind to $\alpha_v\beta_3$ integrin, a well-known tumor biomarker, for tumor targeting, and a $^1O_2$-labile furan module for RNA cross-linking. Once probes *f*-CR were selectively internalized into cancer cells through the specific binding of cRGD to $\alpha_v\beta_3$ integrin, they could spontaneously and covalently cross-link to the cytoplasmic RNAs via the cycloaddition reaction between furan and adenine, cytosine or guanine nucleobases under the oxidation of $^1O_2$ produced on-demand upon the 660 nm light-illumination of photosensitizer methylene blue (MB). Both in vitro and in vivo studies demonstrated that this RLIPRC strategy could efficiently block the exocytosis of probes resulting in improved tumor accumulation and retention. Moreover, it was surprisingly found that the modification of cytoplasmic RNAs by *f*-CR could remarkably induce the apoptosis of cancer cells leading to the effective suppression of 4T1 breast tumor. Hence, these unique features make the probes very advantageous for long-term tumor imaging and antitumor growth and provide new insight for tumor theranostics.

RESULTS AND DISCUSSION

The probes were rationally designed and synthesized through the synthetic route shown in Scheme S1 in Supporting Information (SI) according to our previously reported protocol.[76] In brief, the Boc group on the side chain of Fmoc-Lys (Boc)-COOH was first removed by trifluoroacetic acid (TFA) followed by acylation with *N*-hydroxysuccinimide (NHS)-activated 3-(2-furyl) propanoic acid to afford compound **1**. Next, the carboxyl group of compound **1** was activated by 1-(3-(dimethylamino)propyl)-3-ethylcarbodiimide hydrochloride (EDC·HCl) and NHS, and then reacted with amine-functionalized cRGD through the amidation reaction to yield compound **2**. Subsequent Fmoc deprotection yielded the corresponding amine **3** which was further reacted with cyanine 7 NHS ester (Cy7-NHS) to afford the desired probe *f*-CR with a total yield of 21%. For the purpose of comparison, a control probe CR without a furan unit was also synthesized according to the same synthetic method mentioned above (Figure 1a). CR is theoretically not reactive to adenine, cytosine, or guanine nucleobases of RNA under the

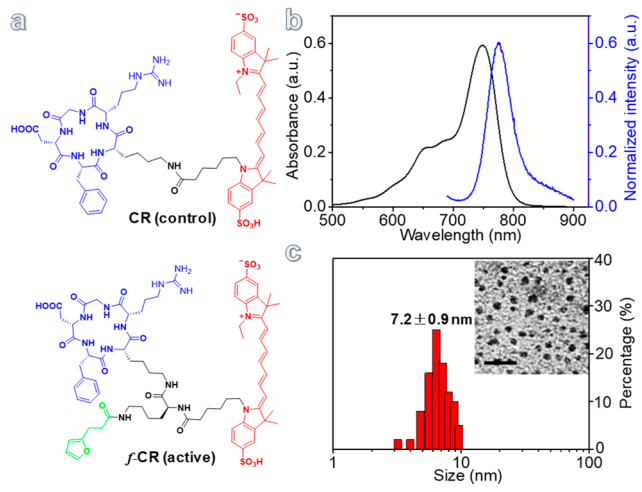

Figure 1. Chemical characterization of probes. (a) The chemical structure of probe CR and *f*-CR. (b) Absorption and fluorescence spectra of *f*-CR (10 μM) in water. (c) TEM characteristic and size distribution of *f*-CR (scale bar = 20 nm).

https://dx.doi.org/10.1021/jacs.0c10755
J. Am. Chem. Soc. 2020, 142, 21502−21512

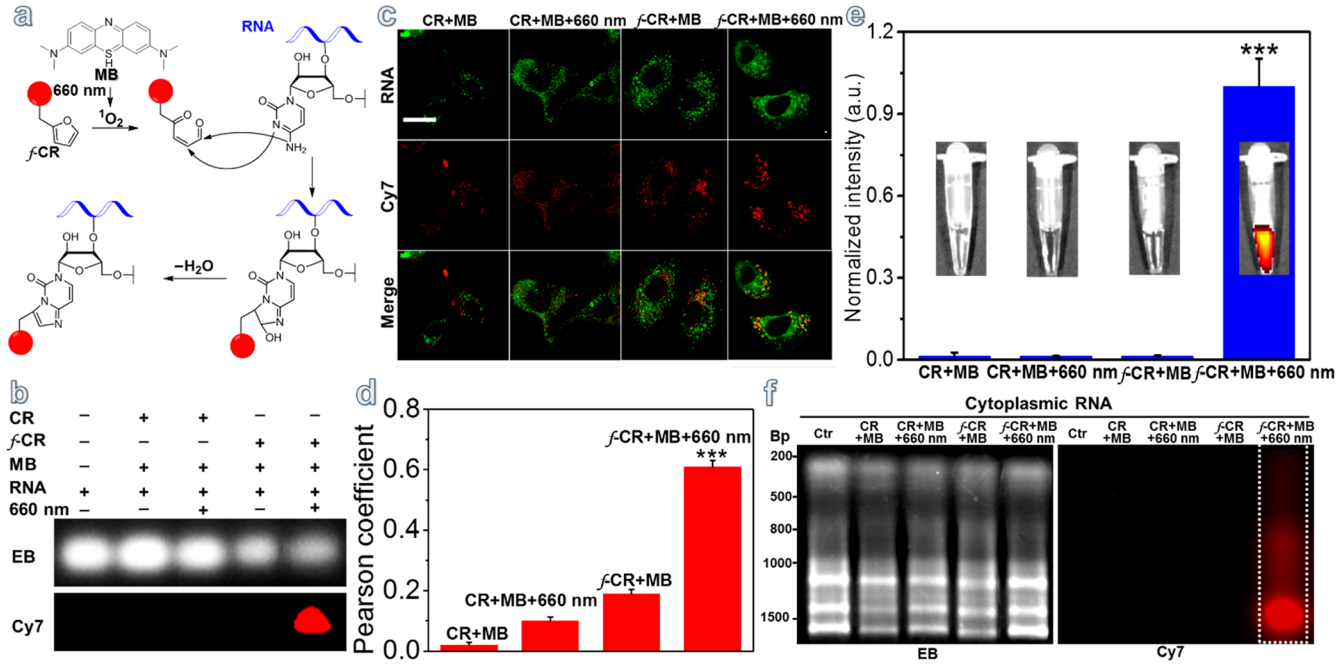

Figure 2. Evaluation of red light-initiated cross-linking capability of probes toward RNA in vitro. (a) The possible mechanism of 660 nm light-initiated cross-linking of *f*-CR to RNA. (b) RNA agarose gel electrophoresis images of different assays under the excitation of 546 nm (EB) and 632 nm (Cy7), respectively. [*f*-CR] = [CR] = [MB] = 10 μM, [RNA] = 20 μM, 660 nm laser: 50 mW/cm^2, 2 min. (c) CLSM images of 4T1 cells receiving different combination treatments and stained by SYTO RNASelect Green (scale bar = 10 μm). [*f*-CR] = [CR] = 5 μM, [MB] = 0.1 μM, 660 nm laser: 50 mW/cm^2, 3 min. (d) Co-localization coefficient quantification of different groups of 4T1 cells. (e) Normalized fluorescence intensity of the extracted cellular RNAs for previous different groups of cells. (f) RNA agarose gel electrophoresis images of different groups of extracted cellular RNAs under the excitation of 546 nm (EB) and 632 nm (Cy7), respectively. The statistical significance level is ***$p < 0.001$.

oxidation of $^1O_2$. All compounds were eventually purified by preparative high-performance liquid chromatography (HPLC) and characterized by high resolution mass spectrometry (HR-MS; Figure S1−S5).

The optical property of probes in aqueous solution was first characterized. As shown in Figures 1b and S6a, both *f*-CR and CR show substantially uniform absorption and emission profiles with the same maximal peaks at 747 and 778 nm, respectively, which is attributed to Cy7 dye, indicating that the probes have good potential for NIR fluorescence and PA imaging (Figure S6c). Additionally, the amphiphilic probe *f*-CR could self-assemble into small nanoparticles spontaneously in aqueous buffer due to the hydrophobic furan and hydrophilic units (such as cRGD and Cy7). The average size of the resulting nanoparticles was 7.2 ± 0.9 nm, as shown in Figure 1c, according to transmission electron microscopy (TEM) measurement, while the hydrodynamic size determined by dynamic light scattering (DLS) was 8.0 ± 0.9 nm (Figure S7). The formation of the *f*-CR particles was further verified through absorption measurement. The absorption spectra of *f*-CR in DMSO with different volume fractions of PBS buffer were recorded. With the increasing fractions of PBS, the maximum absorbance of *f*-CR gradually blue-shifted from 795 to 750 nm, but the intensity remained unchanged when PBS fraction was increased to 90% (Figure S8), indicating that the solvent polarity has a strong impact on the solubility of *f*-CR and PBS buffer can induce *f*-CR to form *H*-type aggregates via an intermolecular $\pi-\pi$ stacking interaction.[77] However, no obvious self-assembly was observed from TEM images of control probe CR, which may be due to its good water solubility (Figure S9). The chemical stability of probe *f*-CR in serum solution was studied by monitoring their absorption spectra and hydrodynamic size over time. The results shown in Figure S10 indicate that probe *f*-CR has great chemical stability in serum aqueous solution.

To evaluate the red light-initiated cross-linking capability of probes toward RNA in aqueous solution, a model single-stranded small RNA was synthesized (Table S1), and a clinically used drug MB was chosen as a photosensitizer to provide $^1O_2$ under laser irradiation. The mixture of probe *f*-CR and RNA was irradiated by 660 nm laser light in the presence of MB (10 μM) for 2 min as experimental group, while probe CR with RNA and MB upon 660 nm illumination, *f*-CR with RNA and MB without irradiation were set as control groups. After 3 min incubation, all the assays were directly analyzed by nondenaturing agarose gel electrophoresis, and visualized by EB staining (E_x = 510 nm) and in-gel fluorescence scanning (E_x = 632 nm). As shown in Figure 2b, strong fluorescent signals were solely determined from RNA band in the experimental assay, whereas almost no fluorescent band was observed from other control groups, implying that the synthetic RNA can be efficiently labeled by *f*-CR through the red light-initiated cross-linking reaction, which was further confirmed by mass spectrometry analysis (Figure S11). Moreover, the cross-linking efficiency of *f*-CR to RNA was demonstrated to be $^1O_2$-dependent, and it can be well controlled by adjusting the concentration of MB (1 μM, 5 μM, and 10 μM) used in the assays (Figure S12). Collectively, all above evidence firmly demonstrate that the $^1O_2$-mediated cross-linking reaction between furan and the NH_2 group of adenine, cytosine, or guanine in RNA took place upon 660 nm laser irradiation.

To investigate the targeting ability of probes to cancer cells, mouse breast carcinoma 4T1 cell was chosen as $\alpha_v\beta_3$ integrin

https://dx.doi.org/10.1021/jacs.0c10755
J. Am. Chem. Soc. 2020, 142, 21502−21512

overexpressed cancer cells, while fibroblast cell line 3T3 expressing a low level of $\alpha_v\beta_3$ integrin was taken as a negative control. The same amount of probe *f*-CR was first incubated with 4T1 and 3T3 cells, respectively, for 3 h followed by confocal laser scanning microscopy (CLSM) imaging. As shown in Figure S13a,b, 4T1 cells exhibited almost 3.1-fold higher red fluorescence than 3T3 cells, implying that *f*-CR has great specificity and targeting capability to $\alpha_v\beta_3$ integrin overexpressed cancer cells. Additionally, the same amount of *f*-CR and CR was treated to 4T1 cells, respectively, at 37 °C for different time (3, 6, 12, and 24 h) incubation, and then their cellular uptake was evaluated by measuring the fluorescent signals of the cellular lysates. The results given in Figure S14 show that intensive fluorescence was observed from both groups of cells, and the fluorescence intensities were gradually strengthened with the increase of incubation times, indicating that probe *f*-CR and CR have similar uptake in 4T1 cells. Next, we studied the phototoxicity of photosensitizer MB to 4T1 cells. Different concentrations of MB ranging from 0.05 to 100 μM were incubated with 4T1 cells for 6 h followed by 660 nm laser irradiation (50 mW/cm^2, 3 min). The cell viability was measured by the methyl thiazolyl tetrazolium (MTT) assay. The results in Figure S15 show that the phototoxicity of MB to 4T1 cells increases dramatically along with increased concentrations of MB treated. The cell survival rate was higher than 98% when MB concentration was below 0.1 μM, suggesting that 0.1 μM of MB used is safe for living cells. To assess the $^1O_2$ production efficiency of MB under 660 nm light irradiation, we then carried out the dihydroethidium (DHE) staining assay to quantify the intracellular $^1O_2$ level. As expected, the production of $^1O_2$ gradually increased as the concentration of MB increases (Figure S16).

To further validate the RLIPRC capability of probe *f*-CR to RNAs in living cells, 4T1 cells were incubated with *f*-CR (10 μM) and MB (0.1 μM) at 37 °C for 6 h followed by 660 nm laser irradiation (denoted as *f*-CR+MB+660 nm) as the experimental group, while the cells treated with *f*-CR and MB without laser irradiation (denoted as *f*-CR+MB), the cells treated with CR and MB followed by 660 nm laser irradiation (denoted as CR+MB+660 nm), and the cells receiving CR and MB without laser irradiation (denoted as CR+MB) were set as control groups. As shown in Figure 2c, the strongest red fluorescence was determined in the cells receiving *f*-CR+MB +660 nm. However, only weak fluorescence was recorded for the other three control groups of cells, implying that probe *f*-CR has improved cellular uptake under the irradiation of 660 nm laser light. Besides, all four groups of 4T1 cells were simultaneously treated to SYTO RNASelect green, a commercial RNA stain, followed by CLSM. In comparison to three control groups, the *f*-CR+MB+660 nm group clearly showed great overlap between *f*-CR (red color) and RNA stain (green color). By quantitatively analyzing the overlapping degree of cell images, it was found that the colocalization percentage was 63.4% and 18.9% for *f*-CR+MB+660 nm and *f*-CR+MB, respectively, whereas groups CR+MB+660 nm and CR+MB were only 10.1% and 3.6% (Figure 2d), which should be mainly attributed to the RLIPRC effect of probes *f*-CR that were immobilized onto the intracellular RNAs. Next, to investigate the cellular location of probe *f*-CR, the cells receiving *f*-CR+MB+660 nm were treated to lyso-tracker green, mito-tracker green, and ER-tracker blue, respectively. Since endoplasmic reticulum (ER) is the main organelle for RNA translation and protein synthesis,[78] it was found that the red fluorescence from *f*-CR have the best colocalization with ER tracker (blue color) compared to other two trackers (Figure S17), suggesting that *f*-CR mainly locates at endoplasmic reticulum in cells. The correlation between colocalization of *f*-CR with RNAs and the amount of MB was further investigated. Figure S18 shows the colocalization degree of *f*-CR with intracellular RNAs increases gradually with the increasing amount of MB used. To confirm the specificity of probe *f*-CR to intracellular RNAs, the aforementioned four groups of 4T1 cells with different combination treatments were treated to RNA total extraction kit TRNzol-A$^+$ separately, and the RNAs in the whole cells were extracted and collected according to the traditional method shown in Scheme S2a. As illustrated in Figure 2e, the RNA fraction of the cells with *f*-CR +MB+660 nm apparently showed the highest fluorescence than the ones from the other three control groups of cells. Moreover, the RNAs in the cytoplasm and nucleus were extracted by using cytoplasm and nucleus purification kits (Scheme S2b), respectively, and separated by RNA non-denaturing agarose gel electrophoresis followed by in-gel fluorescence scanning as well as ethidium bromide (EB) staining. As expected, intensive fluorescent bands were observed for the cytoplasmic RNAs from the *f*-CR+MB+660 nm group (Figures 2f and S19). However, almost no fluorescence was determined for the RNA fraction of the nucleus and the samples from other groups (Figure S20), firmly demonstrating that probes of *f*-CR are mainly reacted to cytoplasmic RNAs rather than the ones in the nucleus. The total proteins of the cells in each groups were also isolated by using RIPA lysis buffer under the same condition, and separated by sodium dodecyl sulfate polyacrylamide gel electrophoresis (SDS-PAGE) followed by fluorescence scanning. No fluorescence was observed for all of the samples (Figure S21), indicative of no reactivity between *f*-CR and intracellular proteins. Collectively, all of the above evidence strongly demonstrates that red light in the presence of photosensitizers can spatiotemporally induce the cross-linking of *f*-CR to cytoplasmic RNAs in living cells.

To further evaluate the characteristics of *f*-CR with enhanced cellular uptake and prolonged residence in cancer cells, four groups of 4T1 cells were pretreated to MB (0.1 μM) and then incubated with *f*-CR or control probe CR (5 μM) for 6 h at 37 °C followed by 660 nm laser irradiation (50 mW/cm^2, 3 min). CLSM images shown in Figure 3a indicate that fluorescence intensities of four groups of cells were nearly identical at the initial stage. By contrast, the fluorescence of the cells receiving CR+MB, CR+MB+660 nm, and *f*-CR+MB decayed rapidly over time, whereas the cells with *f*-CR+MB +660 nm kept strong fluorescence even for 48 h (Figure 3a), which was further confirmed by the quantitative results shown in Figure 3b. The cells with *f*-CR+MB+660 nm remained ca. 51% of the initial fluorescent signals after 48 h of incubation. In a sharp contrast, below 4% of the initial signal was preserved for the other three control groups of cells. This could probably be due to the red light-initiated cross-linking of probe *f*-CR to cytoplasmic RNAs resulting in improved uptake and prolonged residence time in cancer cells.

Inspired by the above exciting results, the RLIPRC effect of *f*-CR was further assessed in vivo. The generation of $^1O_2$ by irradiation of MB with 660 nm laser light was first validated. In brief, MB (50 μL, 0.1 μM) was intratumorally injected into the subcutaneous 4T1 tumor-bearing BALB/c mice. The tumors were exposed to 660 nm laser (50 mW/cm^2) for 3 min at 1.5 h

https://dx.doi.org/10.1021/jacs.0c10755
J. Am. Chem. Soc. 2020, 142, 21502−21512

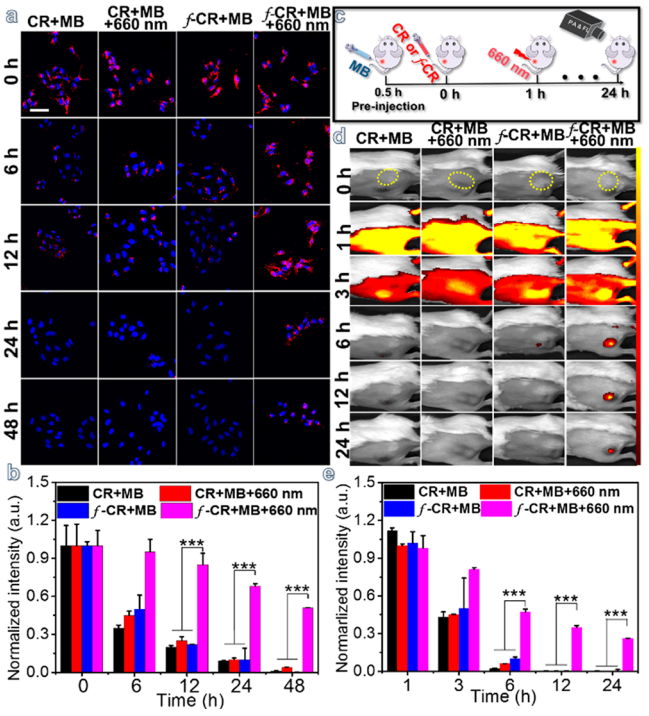

Figure 3. CLSM imaging of 4T1 cells and 4T1 tumor-bearing nude mice. (a) Real-time CLSM images of 4T1 cells with different combination treatments over 48 h. Nuclei were stained with Hoechst 33342 (scale bar = 20 μm). [*f*-CR] = [CR] = 5 μM; [MB] = 0.1 μM; 660 nm laser: 50 mW/cm^2, 3 min. (b) Quantification of fluorescence intensity of 4T1 cells with different treatments over 48 h. (c) Schematic illustration of in vivo PA/NIR dual-modal imaging of 4T1 tumors with different treatments. (d) In vivo real-time fluorescent images of subcutaneous 4T1 tumor-bearing Balb/c female mice with different combination treatments over 24 h. (e) Quantification of fluorescence intensities of tumors with different treatments for 24 h. The statistical significance level is ***$p < 0.001$. [*f*-CR] = [CR] = 100 μM, 200 μL; [MB] = 0.1 μM, 50 μL; 660 nm laser: 50 mW/cm^2, 3 min.

postinjection and then resected for $^1O_2$ detection by DHE staining. As shown in Figure S22, strong fluorescence was determined only from the tumorous tissues with the treatment of MB and 660 nm irradiation, indicative of a high-level production of $^1O_2$. Next, four groups of MB pretreated subcutaneous 4T1 tumor-bearing BALB/c nude mice (n = 3) were intravenously injected with probe *f*-CR or CR at a dosage of 100 μM and 200 μL via tail vein. At 1 h postinjection, the tumorous areas were exposed to 660 nm laser for 3 min followed by NIR imaging using IVIS spectrum (Figure 3c). Time-dependent fluorescent images of various tumors treated with *f*-CR versus control groups are shown in Figures 3d and S23. All groups of tumors exhibited almost identical and high fluorescence at the initial 1 h. As time elapses, the fluorescent signals in all groups of tumors gradually decayed. By contrast, the fluorescence of the control tumors treated with CR+MB, CR+MB+660 nm, and *f*-CR+MB decreased sharply due to the quick clearance from tumors. However, the fluorescence of tumors receiving *f*-CR+MB+660 nm was obviously higher than that of the control groups at each recorded time (3, 6, 12, and 24 h), which is consistent with aforementioned cell imaging results shown in Figure 3a. The quantitative analysis further indicated that the tumors receiving *f*-CR+MB+660 nm at 24 h still retained 26% fluorescent signals of that at 1 h, while the fluorescence intensities of the other three control groups was less than 1% (Figure 3e).

Similarly, the in vivo photoacoustic (PA) imaging in Figure 4a shows that the PA intensities of all groups of tumors were

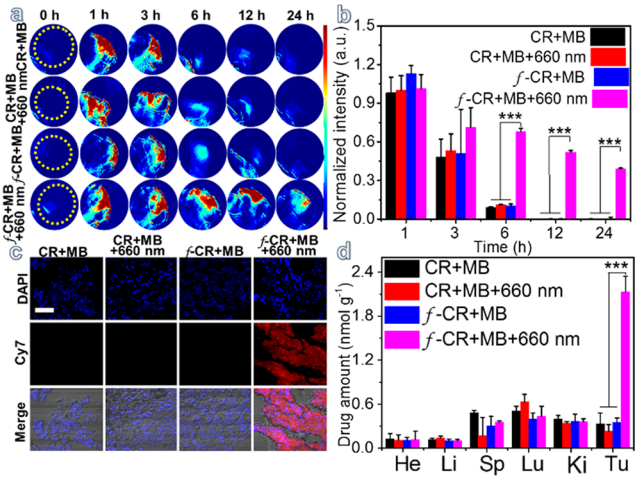

Figure 4. In vivo photoacoustic (PA) imaging of 4T1 tumors and the biodistribution of probes in mice. (a) In vivo PA imaging and (b) quantitative PA intensities of 4T1 tumors with different treatments at different time points. (c) Fluorescent imaging of the tumor tissues receiving different treatments and stained by DAPI (scale bar = 100 μm). (d) The biodistribution of probes in four groups of mice. [*f*-CR] = [CR] = 100 μM, 200 μL; [MB] = 0.1 μM, 50 μL; 660 nm laser: 50 mW/cm^2, 3 min. The statistical significance level is ***$p < 0.001$.

nearly identical at 1 h. In comparison with three control groups, the tumors receiving *f*-CR+MB+660 nm obviously maintained strong PA signal for 24 h. The quantitative analysis of average PA signals in the tumor regions indicated that the tumors with *f*-CR+MB+660 nm were 50-fold higher than that of the other three groups at 24 h (Figure 4b), suggesting that $^1O_2$-initiated cross-linking of probe *f*-CR to cytoplasmic RNAs occurred under illumination of 660 nm light. Fluorescent signal of the resected tumor tissues at 12 h postinjection was further determined ex vivo. Figure 4c shows the tumor tissues of mice receiving *f*-CR+MB+660 nm exhibited obviously the strongest fluorescence among all groups, which is quite consistent with the aforementioned in vivo NIR images. Additionally, an ex vivo biodistribution study indicated that the experimental group of tumors presented around 6-folds higher fluorescence than the other control groups even after 12 h (Figure 4d). Collectively, these results strongly demonstrate that this RLIPRC approach can significantly improve the accumulation and retention of probe *f*-CR in tumors for long-term tumor imaging.

Next, the cytotoxicity of the probes was also assessed by the widely used MTT assay and blood routine analysis. As shown in Figure 5a and 5b, both probe *f*-CR and CR showed negligible cytotoxicity to 4T1 cells in a concentration range of 0.1 to 100 μM as the overall cell viability remained above 85% after 48 h incubation. The blood routine biochemical results indicate that no significant difference for all parameters (WBC, RBC, HGB, HCT, MCV, and PLT) associated with acute toxicity was observed (Figure S24), suggesting probe *f*-CR has good biocompatibility. However, if the above two groups of 4T1 cells were treated with MB (0.1 μM) and the same dose of 660 nm laser irradiation (50 mW/cm^2, 3 min), followed by

https://dx.doi.org/10.1021/jacs.0c10755
J. Am. Chem. Soc. 2020, 142, 21502−21512

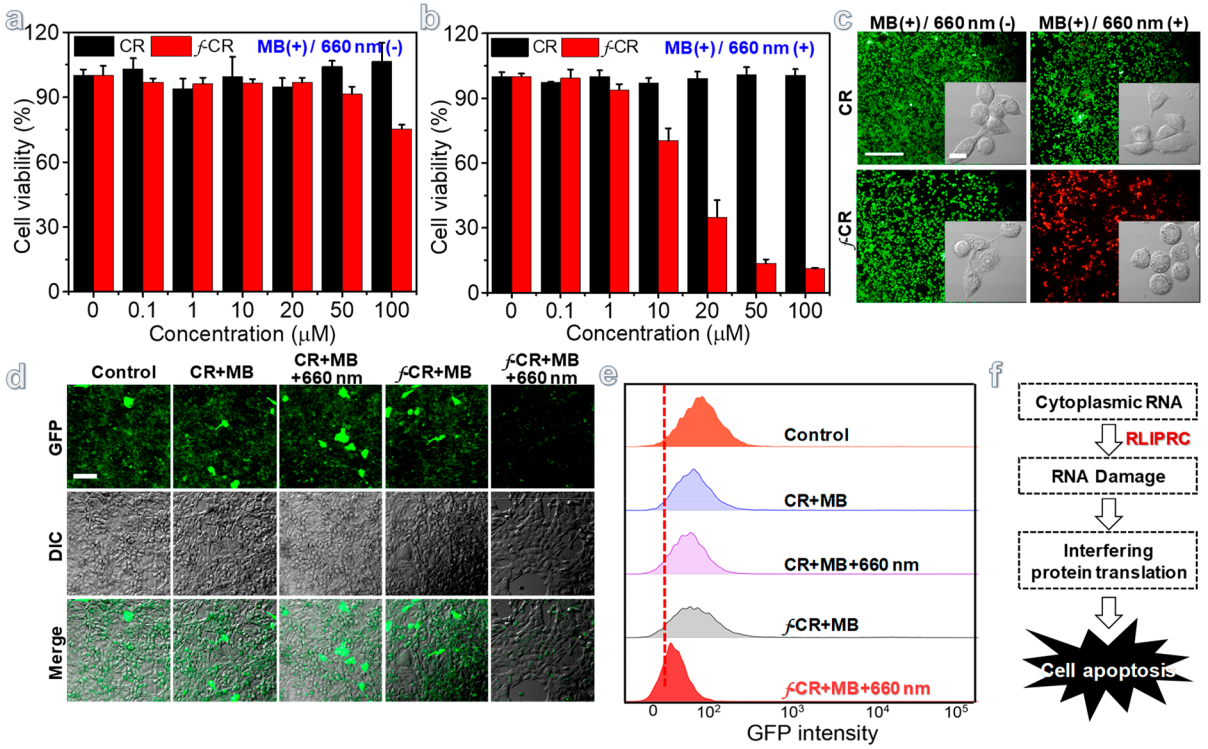

Figure 5. In vitro and in vivo evaluation of the cytotoxic effect of probes to 4T1 cancer cells. (a) Cell viability of 4T1 cells pretreated MB (0.1 μM) and receiving *f*-CR or CR without (a) and with (b) 660 nm laser light irradiation. (c) Fluorescent images of different groups of 4T1 cells with staining of live (green)/dead (red) kit (scale bar = 10 and 100 μm). [*f*-CR] = [CR] = 30 μM; [MB] = 0.1 μM; 660 nm laser: 50 mW/cm^2, 3 min, scale bar = 100 μm. (d) Confocal images of the GFP expression for different groups of 4T1 cells (scale bar = 100 μm). (e) Flow cytometry results of the aforementioned groups of cells. (f) The possible mechanism of the RLIPRC-based cancer cell suppression.

MTT characterization, a remarkable cell death was surprisingly observed only for the cells receiving *f*-CR above 10 μM. In contrast, no evident cytotoxicity was determined for the cells with CR even in a concentration of 100 μM. The cytotoxic effect of probe *f*-CR on 4T1 cells was further characterized through live/dead staining. The results given in Figure 5c showed that the cells were effectively killed on subjection to *f*-CR+MB+660 nm accompanied by obvious morphological change, otherwise no evident cell death was observed for the other three control groups of cells (Figure S25). The apoptotic rate was also examined by using flow cytometry. As expected, the apoptotic level of the cells with *f*-CR+MB+660 nm was up to 84%, while the other three control groups of cells were less than 1.7% (Figure S26). We envisioned that the cross-linking of *f*-CR to cytoplasmic RNAs could affect the cell proliferation leading to severe cell apoptosis.

To validate our above hypothesis, we employed a commercially available GFP-mRNA as a model RNA to study the effect of probe *f*-CR on GFP expression in living cells. The GFP-mRNA was separately treated with PBS alone (denoted as the control), a mixture of probe CR and MB (denoted as CR+MB), a mixture of CR and MB followed by 660 nm irradiation (denoted as CR+MB+660 nm), a mixture of probe *f*-CR and MB (denoted as *f*-CR+MB), and a mixture of probe *f*-CR and MB followed by 660 nm irradiation (denoted as *f*-CR+MB+660 nm). These pretreated GFP-mRNAs were then transfected into different groups of 4T1 cells using a Hieff Trans liposomal transfection reagent. The cells were cultured for an additional 24 h and subsequently analyzed by confocal microscopy and flow cytometry to assess the expression efficiency of GFP. As shown in Figure 5d,e, as compared with the other four control groups of cells, the cells with *f*-CR+MB+660 nm showed remarkably lower green fluorescence, indicative of low GFP expression. Hence, we speculate that the biological function of the cytoplasmic RNAs that were modified by probe *f*-CR may be interfered, which causes the abnormal protein expression resulting in severe cell apoptosis (Figure 5f).

In light of these exciting results, the in vivo tumor suppression performance of probe *f*-CR was further validated. As shown in Scheme S3, BALB/c mice bearing two 4T1 tumors (~90 mm^3) on both the left and right back were randomly divided into three groups (n = 5), and were intratumorally administrated with 50 μL of aqueous solution of MB (0.1 μM) first. At 0.5 h postinjection, the tumors in each group of mice were subjected to different combinations of treatments in which tumor receiving PBS (denoted as control, group 1), tumor receiving PBS followed by 660 nm irradiation (denoted as control+660 nm, group 2), tumor receiving CR and MB (denoted as CR+MB, group 3), tumor receiving CR and MB followed by 660 nm irradiation (denoted as CR+MB +660 nm, group 4), and tumor receiving *f*-CR and MB (denoted as *f*-CR+MB, group 5) were set as control groups, for showing the tumor suppression efficacy of the experimental group *f*-CR plus MB and 660 nm irradiation (denoted as *f*-CR +MB+660 nm, group 6). The tumor suppression was evaluated by monitoring the average tumor size of different groups over a period of 13 days. The tumors grew rapidly in a similar way for control groups 1 to 5 with a rather weak inhibition of tumor growth (Figures 6a,b and S27). In huge contrast, the tumors receiving *f*-CR+MB+660 nm were significantly reduced in size with around 70% tumor suppression on day 13. The tumor

https://dx.doi.org/10.1021/jacs.0c10755
J. Am. Chem. Soc. 2020, 142, 21502−21512

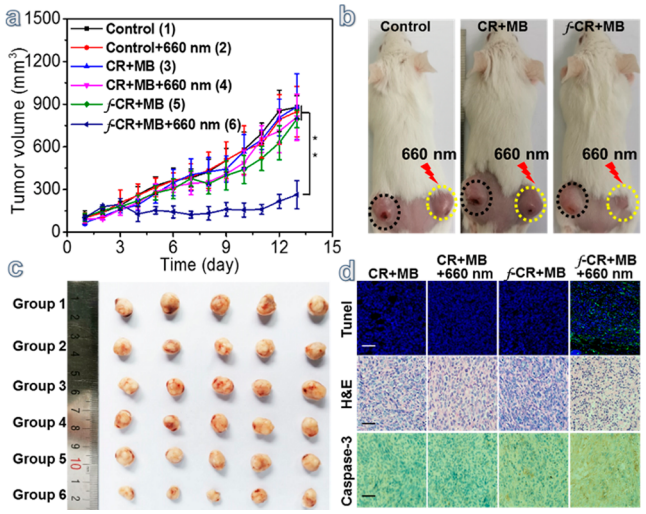

Figure 6. In vivo evaluation of the tumor suppression. (a) Tumor growth profiles of the mice treated to PBS (control), CR or *f*-CR in the presence of MB (0.1 μM, 50 μL) with or without 660 nm light irradiation (50 mW/cm^2, 3 min), the mice photos at day 13 (b), and tumor photos (c). (e) Tunnel staining, H&E and caspase 3 staining images of tumorous tissues treated with CR or *f*-CR (500 μM, 200 μL) in the presence MB (0.1 μM, 50 mL) with or without 660 nm light irradiation (50 mW/cm^2, 3 min; scale bar = 50 μm). The statistical significance level is $^{**}p < 0.01$.

volume and body weight of each mouse in the control groups were 2-fold bigger than the ones in the experimental group (Figures 6c and S28). Moreover, the tumorous tissues were extracted at 48 h postirradiation of 660 nm laser and subjected to hematoxylin and eosin (H&E) staining. Qualitative histological examination of the tumor slices showed that no obvious malignant necrosis was observed for three control groups of tumors, while the *f*-CR+MB+660 nm group clearly had the highest necrotic rate among all test groups. The TUNEL assay and immuno-histochemical staining of activated caspase-3 were also performed for above tumorous tissues to assess the extent of tumor apoptosis. Compared with three control groups, significant DNA damage and a high level of activated caspase-3 expression were determined from the tumor tissues receiving *f*-CR+MB+660 nm (Figure 6d), suggesting an effective suppression of tumor cell proliferation. Collectively, all of this evidence firmly demonstrates that the unexpected therapeutic effect endowed by red light-initiated cross-linking of probe *f*-CR to cytoplasmic RNA makes it promising for efficient cancer therapy.

CONCLUSION

In summary, a red light-initiated site-specific cross-linking strategy was for the first time exploited here to robustly enhance the tumor imaging and achieve unexpected tumor suppression. Both in vitro and in vivo studies have demonstrated that probe *f*-CR has great tumor targeting capability and emits intensive NIR/PA dual-modal signals, allowing for specific and sensitive visualization of tumors in vivo. Notably, this probe could be specifically cross-linked to cytoplasmic RNAs under the oxidation of $^1O_2$ generated in situ by irradiation of MB with 660 nm laser, which can dramatically improve the accumulation and retention of probes in tumors for prolonged tumor imaging. More surprisingly, the covalent cross-linking of probe *f*-CR to cytoplasmic RNAs was demonstrated to remarkably induce cell apoptosis leading to significant tumor suppression. This study represents the first red light-mediated RNA cross-linking system with high potential for cancer imaging and therapy. Therefore, we envision that the current approach may offer an attractive tool for long-term cancer imaging and highly efficient tumor therapy.

EXPERIMENTAL SECTION

General Information. The peptide cRGD and amino acid Boc-Lys(Fmoc)−OH were purchased from GL Biochem (Shanghai, China). Single-stranded small RNA and GFP-mRNA was synthesized by GenePharma (Suzhou, China) as requested. Cy7-SE was purchased from Click Chemistry Tools (Scottsdale, AZ). 3-(2-Furyl) propanoic acid, methylene blue, TRNzol-A$^+$ reagent, and MTT kit were purchased from Sigma-Aldrich (St. Louis, MO). SYTO RNASelect green fluorescent cell stain and LIVE/DEAD viability/cytotoxicity kit were purchased from Thermo Fisher (Eugene, OR). The cytoplasmic and Nuclear RNA Purification Kit was purchased from NORGEN Biotek (ON, Canada). Annexin V-FITC/PI Kit was bought from Beyotime (Shanghai, China). Caspase-3 antibody was purchased from Cell Signaling (Danvers, MA). All Western blot reagents were purchased from Beyotime (Shanghai, China). All chemical reagents used in the synthesis of the probes were obtained from Sigma-Aldrich (St. Louis, MO) and used without any further purification. Milli-Q water with a resistivity above 18 MΩ cm was used in the experiments.

HPLC profiles were acquired by using 1260 high performance liquid chromatography (Agilent). HR-MS was obtained on a 6230 time-offlight mass spectrometer and a 6540 UHD accurate-mass quadrupole time-of-flight mass spectrometer (Agilent). UV−vis absorption spectra were measured on PerkinElmer LAMBDA 750. The fluorescence spectra were measured on an Edinburgh FLS980 spectrophotometer. Dynamic light scattering (DLS) measurements were performed on a particle size analyzer (Nano ZS90, Malvern) at 25 °C. TEM images were acquired by electron microscope (Tecnai G2 Spirit, FEI) spectrophotometer. Gel electrophoresis was conducted through BIO-RAD 1645050 and images were obtained by Gel Doc EZ Imager (BIO-RAD). The in vivo fluorescence images were acquired using an IVIS spectrum imaging system (PerkinElmer). The confocal images were captured on a fluorescence microscope (FV1200, Olympus). PA imaging was obtained through a multi-spectral optoacoustic tomography (MSOT).

Preparation and Characterization of Probe *f*-CR in Aqueous Solution. A total of 1 mg of *f*-CR dissolved in 1 mL of DMSO was dispersed into distilled water under ultrasoniccation followed by dialysis for 24 h to remove DMSO. The hydrodynamic diameter was measured on Zetasizer ZS90 (Malvern, UK). The morphology was characterized by TEM measurement (Tecnai G20).

Absorption and Fluorescence Spectra Measurements. The absorption and fluorescence spectra of *f*-CR and CR (10 μM) were recorded by UV−vis and fluorescence spectrophotometers, respectively.

In Vitro Study of Red Light-Initiated Cross-Linking of Probes to RNA. *f*-CR and CR (10 μM, 10 μL) were first mixed with 10 μL of methylene blue (10 μM), respectively, and then incubated with 5 μL of RNA (10 μM) for 0.5 h at 4 °C. Subsequently, the mixtures were exposed to 660 nm laser light irradiation (50 mW/m^2) for 2 min with 1000 rpm shaking at 4 °C. The control assays were treated with the same condition except for light irradiation. All the solutions were loaded onto analytical nondenaturing agarose gel electrophoresis and ran in 1× MOPS buffer at 200 V for 40 min. Finally, the gels were dried and the data was recorded on a UVP BioSpectrum Imaging System and IVIS spectrum.

Cellular Uptake. 4T1 cells were seeded in the six-well plates (7 × 10^5 cell/well) and incubated in RPMI 1640 containing 10% FBS for 12 h. Then, 100 μM *f*-CR and CR were added into the wells, respectively. After 3, 6, 12, and 24 h incubation, the cells were washed with PBS for three times and then incubated with trypsin (0.5 mL/

https://dx.doi.org/10.1021/jacs.0c10755
J. Am. Chem. Soc. 2020, 142, 21502−21512

well) for 3 min followed by cell counting. The collected cells were lysed under ultrasonication and put in a −80 °C refrigerator for 12 h. After lyophilizing, the cells were dissolved into DMSO and centrifugated. The supernatant was used for fluorescence spectrophotometer analysis.

Intracellular Distribution. 4T1 cells (2×10^5 cells/well) were seeded in a glass dish for 12 h. CLSM was then employed to study the intracellular distribution of *f*-CR and CR. Briefly, the cells were first treated with MB (0.1 μM) and then incubated with *f*-CR or CR at a dose of 5 μM. After 6 h of incubation at 37 °C, the cells were washed by PBS buffer for three times. Afterward, the cells were treated with or without 660 nm irradiation (50 mW/cm^2) for 3 min followed by Hoechst 33342 (500 μL, 10 μg/mL) or SYTO RNaselect Green (500 μL, 500 nM) staining for 15 min at 37 °C. CLSM was finally carried out to visualize the intracellular distribution of *f*-CR and CR.

Extraction of Intracellular RNAs from the Whole Cells. MB-pretreated 4T1 cells were incubated with *f*-CR or CR (5 μM) for 6 h at 37 °C. After changing to the fresh medium, the cells were irradiated by 660 nm laser (50 mW/cm^2) for 3 min and then treated to Trizol kit or cytoplasmic and nuclear RNA purification kit to extract the cytoplasimic RNAs and RNAs in nucleu. The RNA fractions were eventually ran RNA gel electrophoresis.

Assessment of $^1O_2$ Generation Using Dihydroethidium (DHE) Staining. 4T1 cells (2×10^6 cells/well) were seeded into the 12-well plates and grew in RPMI 1640 containing 10% FBS. Different concentrations of MB (50 μL, 0.01, 0.05, and 0.1 μM) was added into the wells, and incubated for 6 h at 37 °C. The cells were then washed using PBS for three times, and further treated to 660 nm irradiation (50 mW/cm^2) for 3 min. Afterward, the cells were incubated with DHE (10 μM) for 5 min at 37 °C, and washed by PBS for three times. The cells were finally visualized by fluorescence microscope to assess the amount of $^1O_2$ generated.

Intracellular Retention Study of Probes. 4T1 cells (2×10^6 cells/well) were cultured in glass dishes for 12 h and then treated with MB (0.1 μM) first. Probe *f*-CR or CR at a dose of 5 μM were added into the cells and incubated for 6 h at 37 °C. After PBS washing, the cells were subsequently exposed to 660 nm irradiation (50 mW/cm^2) for 3 min or not. Real-time imaging of the cells was eventually performed by CLSM at 3, 6, 12, 24, and 48 h.

In Vitro Photocytotoxicity Study. 4T1 cells (1.0×10^4 cells/well) were seeded in 96-well plates and cultured in 1640 rpmI medium containing 10% FBS for 12 h at 37 °C. Different concentrations of MB (0, 0.05, 0.1, 1, 10, 20, 50, and 100 μM) were then added into the cells followed by 660 nm irradiation (50 mW/cm^2) for 3 min. After 24 h of growing, the cell viability was evaluated using MTT assay. To evaluate the cytotoxicity of *f*-CR and CR on 4T1 cells, MB (0.1 μM) pretreated 4T1 cells were incubated with different concentrations (0.05, 0.1, 1, 10, 20, 50, and 100 μM) of *f*-CR or CR. After 12 h incubation at 37 °C, the cells were exposed to 660 nm laser irradiation (50 mW/cm^2) for 3 min and then cultured for a further 48 h. The cell viability was evaluated using MTT assay.

In Vitro Cytotoxicity Study. Probe *f*-CR or CR (30 μM) was incubated with MB-pretreated 4T1 cells for 12 h at 37 °C. After changing to fresh medium, the cells were irradiated by 660 nm laser (50 mW/cm^2) for 3 min. After incubation for further 48 h, the cell morphology and live/dead cells were visualized by fluorescence microscope using a live−dead kit. The cell apoptosis was also analyzed by flow cytometry using Annexin V-FITC/PI kit.

Evaluation of RISCL Effect on GFP Expression. *f*-CR or CR (10 μM) was mixed with GFP-mRNA (2 μM) and MB (10 μM) at 4 °C. The mixture was then treated with or without 660 nm irradiation (50 mW/m^2) accompanied by shaking at 4 °C. The reaction mixture was subsequently transfected into 4T1 cells using Hieff TransTM liposomal transfection reagent and cultured for 24 h. The GFP expression was analyzed by confocal microscopy and flow cytometry.

In Vivo NIR Imaging of 4T1 Tumors. 4T1 cells (2×10^6/mice) were implanted into the right side back of female balb/c mice. When the tumors reached to 80−100 mm^3, MB (50 μL, 0.1 μM) was intratumorally injected into the mice. After 30 min, probes *f*-CR and CR (200 μL, 100 μM) were intravenously injected into two groups of 4T1 tumor-bearing mice via tail vain, respectively. At 1 h postinjection, the tumors were exposed to 660 nm laser light (50 mW/cm^2) for 3 min. The mice were then imaged by IVIS at several time points (1, 3, 6, 12, and 24 h). The tumors at 2 h were extracted and frozen at −80 °C and sliced into 10 mm thick slices using freezing microtome for CLSM. The mice were sacrificed after 12 h. The tissues of major organs including heart, liver, spleen, lung, kidney, and tumor were collected and homogenated in tube. Next, 2 mL of DMSO was added into the tube, and the solutions were centrifuged at 10 000 rpm for 15 min. The supernatant was lyophilized and further dissolved in 0.3 mL of DMSO solvent. Afterward, all samples were measured by fluorescence spectrophotometer.

In Vivo Photoacoustic Imaging of 4T1 Tumors. When tumors reached 80−100 mm^3, MB was first intratumorally injected into bearing 4T1 tumor mice. After 30 min, probe *f*-CR and CR (200 μL, 100 μM) were intravenously injected into the 4T1 tumor-bearing mice via tail vain. At 1 h postinjection, the tumors were exposed to 660 nm laser light (50 mW/cm^2) for 3 min. The tumors were then imaged by MSOT (multispectral optoacoustic tomography).

In Vivo Evaluation of $^1O_2$ Production Using DHE Staining. MB (50 μL, 0.1 μM) was in intratumorally injected into 4T1 tumor-bearing mice. After 1.5 h, the tumors were irradiated by a 660 nm laser (50 mW/cm^2) for 3 min followed by extraction and freezing in −80 °C. The tumors were sliced into 10 mm thick slices by using freezing microtome. The slices were finally imaged by a fluorescence microscope.

In Vivo Antitumor Study. MB (0.1 μM, 50 μL) was first intratumorally injected into the tumors in BALB/c mice bearing two 4T1 tumors (~90 mm^3) on both left and right back. After 30 min, probe *f*-CR and CR (500 μM, 200 μL) were intravenously injected into two groups of mice via the tail vain, respectively. At 1 h postinjection, the right side of tumors was irradiated by 660 nm laser (50 mW/cm^2) for 3 min. The tumor size was then measured every day, and the mice were sacrificed on the 13th day.

■ ASSOCIATED CONTENT

Supporting Information

The Supporting Information is available free of charge at https://pubs.acs.org/doi/10.1021/jacs.0c10755.

Synthetic methods, synthetic routes, characterizations of all compounds; UV absorption of CR and TEM of control group; Cy7 fluorescence intensity standard curve; photoacoustic signal intensity of *f*-CR solutions at different concentrations; hydrated particle size distribution of *f*-CR; mass spectrum data after *f*-CR-RNA cross-linking; cross-linking efficiency under the different MB concentrations; difference of *f*-CR uptake in 3T3 and 4T1 cells; cells uptake changes of probes at different time points; cytotoxicity of MB; the capability of MB to produce ROS; electrophoresis to investigate RNA in the nucleus; protein electrophoresis to investigate the total proteins in the whole cell; fluorescence intensity change of tumors in vivo at different time points; apoptotic evaluation; weight measurement of the isolated tumor after the different combination treatments, including Schemes S1−S3, Figures S1−S28, Table S1, and RNA information (PDF)

■ AUTHOR INFORMATION

Corresponding Author

Haibin Shi − *State Key Laboratory of Radiation Medicine and Protection, School for Radiological and Interdisciplinary Sciences (RAD-X) and Collaborative Innovation Center of Radiation Medicine of Jiangsu Higher Education Institutions,*

https://dx.doi.org/10.1021/jacs.0c10755
J. Am. Chem. Soc. 2020, 142, 21502−21512

Soochow University, Suzhou 215123, P. R. China; orcid.org/0000-0003-2234-9126; Email: hbshi@suda.edu.cn

Authors

Shuyue Ye − *State Key Laboratory of Radiation Medicine and Protection, School for Radiological and Interdisciplinary Sciences (RAD-X) and Collaborative Innovation Center of Radiation Medicine of Jiangsu Higher Education Institutions, Soochow University, Suzhou 215123, P. R. China*

Chaoxiang Cui − *State Key Laboratory of Radiation Medicine and Protection, School for Radiological and Interdisciplinary Sciences (RAD-X) and Collaborative Innovation Center of Radiation Medicine of Jiangsu Higher Education Institutions, Soochow University, Suzhou 215123, P. R. China*

Xiaju Cheng − *Jiangsu Key Laboratory of Infection & Immunity, Institutes of Biology & Medical Sciences, Soochow University, Suzhou 215123, P. R. China*

Meng Zhao − *State Key Laboratory of Radiation Medicine and Protection, School for Radiological and Interdisciplinary Sciences (RAD-X) and Collaborative Innovation Center of Radiation Medicine of Jiangsu Higher Education Institutions, Soochow University, Suzhou 215123, P. R. China*

Qiulian Mao − *State Key Laboratory of Radiation Medicine and Protection, School for Radiological and Interdisciplinary Sciences (RAD-X) and Collaborative Innovation Center of Radiation Medicine of Jiangsu Higher Education Institutions, Soochow University, Suzhou 215123, P. R. China*

Yuqi Zhang − *State Key Laboratory of Radiation Medicine and Protection, School for Radiological and Interdisciplinary Sciences (RAD-X) and Collaborative Innovation Center of Radiation Medicine of Jiangsu Higher Education Institutions, Soochow University, Suzhou 215123, P. R. China*

Anna Wang − *State Key Laboratory of Radiation Medicine and Protection, School for Radiological and Interdisciplinary Sciences (RAD-X) and Collaborative Innovation Center of Radiation Medicine of Jiangsu Higher Education Institutions, Soochow University, Suzhou 215123, P. R. China*

Jing Fang − *State Key Laboratory of Radiation Medicine and Protection, School for Radiological and Interdisciplinary Sciences (RAD-X) and Collaborative Innovation Center of Radiation Medicine of Jiangsu Higher Education Institutions, Soochow University, Suzhou 215123, P. R. China*

Yan Zhao − *State Key Laboratory of Radiation Medicine and Protection, School for Radiological and Interdisciplinary Sciences (RAD-X) and Collaborative Innovation Center of Radiation Medicine of Jiangsu Higher Education Institutions, Soochow University, Suzhou 215123, P. R. China*

Complete contact information is available at: https://pubs.acs.org/10.1021/jacs.0c10755

Notes

The authors declare no competing financial interest.

■ ACKNOWLEDGMENTS

We acknowledge financial support from the Training Program of the Major Research Plan of the National Natural Science Foundation of China (91959123), Key Research and Development Program of Social Development of Jiangsu Province (BE2018655), the National Science Foundation of China (22077092), the Open Project Program of the State Key Laboratory of Radiation Medicine and Protection (GZK1202017, GZK1201916), and a project funded by the Priority Academic Program Development of Jiangsu Higher Education Institutions. Dedicated to the 120th anniversary of Soochow University and the 20th anniversary of Prof Shun-Jun Ji's research group.

■ REFERENCES

(1) Zhao, N.; Yan, L.; Zhao, X.; Chen, X.; Li, A.; Zheng, D.; Zhou, X.; Dai, X.; Xu, F. J. Versatile Types of Organic/Inorganic Nanohybrids: From Strategic Design to Biomedical Applications. *Chem. Rev.* **2019**, *119*, 1666−1762.

(2) Li, H.; Yao, Q.; Sun, W.; Shao, K.; Lu, Y.; Chung, J.; Kim, D.; Fan, J.; Long, S.; Du, J.; Li, Y.; Wang, J.; Yoon, J.; Peng, X. Aminopeptidase N Activatable Fluorescent Probe for Tracking Metastatic Cancer and Image-Guided Surgery via in Situ Spraying. *J. Am. Chem. Soc.* **2020**, *142* (13), 6381−6389.

(3) Bandara, N.; Sharma, A. K.; Krieger, S.; Schultz, J. W.; Han, B. H.; Rogers, B. E.; Mirica, L. M. Evaluation of (64)Cu-Based Radiopharmaceuticals that Target Abeta Peptide Aggregates as Diagnostic Tools for Alzheimer's Disease. *J. Am. Chem. Soc.* **2017**, *139*, 12550−12558.

(4) Goswami, S.; Walle, T.; Cornish, A. E.; Basu, S.; Anandhan, S.; Fernandez, I.; Vence, L.; Blando, J.; Zhao, H.; Yadav, S. S.; Ott, M.; Kong, L. Y.; Heimberger, A. B.; de Groot, J.; Sepesi, B.; Overman, M.; Kopetz, S.; Allison, J. P.; Pe'er, D.; Sharma, P. Immune profiling of human tumors identifies CD73 as a combinatorial target in glioblastoma. *Nat. Med.* **2020**, *26*, 39−46.

(5) Yin, L.; Sun, H.; Zhang, H.; He, L.; Qiu, L.; Lin, J.; Xia, H.; Zhang, Y.; Ji, S.; Shi, H.; Gao, M. Quantitatively Visualizing Tumor-Related Protease Activity in Vivo Using a Ratiometric Photoacoustic Probe. *J. Am. Chem. Soc.* **2019**, *141*, 3265−3273.

(6) Fan, Z.; Sun, L.; Huang, Y.; Wang, Y.; Zhang, M. Bioinspired fluorescent dipeptide nanoparticles for targeted cancer cell imaging and real-time monitoring of drug release. *Nat. Nanotechnol.* **2016**, *11*, 388−394.

(7) Hollon, T. C.; Pandian, B.; Adapa, A. R.; Urias, E.; Save, A. V.; Khalsa, S. S. S.; Eichberg, D. G.; D'Amico, R. S.; Farooq, Z. U.; Lewis, S.; Petridis, P. D.; Marie, T.; Shah, A. H.; Garton, H. J. L.; Maher, C. O.; Heth, J. A.; McKean, E. L.; Sullivan, S. E.; Hervey-Jumper, S. L.; Patil, P. G.; Thompson, B. G.; Sagher, O.; McKhann, G. M., 2nd; Komotar, R. J.; Ivan, M. E.; Snuderl, M.; Otten, M. L.; Johnson, T. D.; Sisti, M. B.; Bruce, J. N.; Muraszko, K. M.; Trautman, J.; Freudiger, C. W.; Canoll, P.; Lee, H.; Camelo-Piragua, S.; Orringer, D. A. Near real-time intraoperative brain tumor diagnosis using stimulated Raman histology and deep neural networks. *Nat. Med.* **2020**, *26*, 52−58.

(8) Jiang, Y.; Huang, J.; Zhen, X.; Zeng, Z.; Li, J.; Xie, C.; Miao, Q.; Chen, J.; Chen, P.; Pu, K. A generic approach towards afterglow luminescent nanoparticles for ultrasensitive in vivo imaging. *Nat. Commun.* **2019**, *10*, 2064.

(9) McHugh, K. J.; Jing, L.; Behrens, A. M.; Jayawardena, S.; Tang, W.; Gao, M.; Langer, R.; Jaklenec, A. Biocompatible Semiconductor Quantum Dots as Cancer Imaging Agents. *Adv. Mater.* **2018**, *30*, 1706356−1706356.

(10) Basuki, J. S.; Esser, L.; Duong, H. T. T.; Zhang, Q.; Wilson, P.; Whittaker, M. R.; Haddleton, D. M.; Boyer, C.; Davis, T. P. Magnetic nanoparticles with diblock glycopolymer shells give lectin concentration-dependent MRI signals and selective cell uptake. *Chem. Sci.* **2014**, *5*, 715−726.

(11) Peng, R.; Xu, L.; Wang, H.; Lyu, Y.; Wang, D.; Bi, C.; Cui, C.; Fan, C.; Liu, Q.; Zhang, X.; Tan, W. DNA-based artificial molecular signaling system that mimics basic elements of reception and response. *Nat. Commun.* **2020**, *11*, 978.

(12) Xu, S.; Liu, H. W.; Chen, L.; Yuan, J.; Liu, Y.; Teng, L.; Huan, S. Y.; Yuan, L.; Zhang, X. B.; Tan, W. Learning from Artemisinin: Bioinspired Design of a Reaction-Based Fluorescent Probe for the Selective Sensing of Labile Heme in Complex Biosystems. *J. Am. Chem. Soc.* **2020**, *142*, 2129−2133.

(13) Zheng, D.-W.; Gao, F.; Cheng, Q.; Bao, P.; Dong, X.; Fan, J.-X.; Song, W.; Zeng, X.; Cheng, S.-X.; Zhang, X.-Z. A vaccine-based

nanosystem for initiating innate immunity and improving tumor immunotherapy. *Nat. Commun.* **2020**, *11*, 1985.
(14) Fan, W.; Yung, B.; Huang, P.; Chen, X. Nanotechnology for Multimodal Synergistic Cancer Therapy. *Chem. Rev.* **2017**, *117*, 13566−13638.
(15) Huang, J.; Li, J.; Lyu, Y.; Miao, Q.; Pu, K. Molecular optical imaging probes for early diagnosis of drug-induced acute kidney injury. *Nat. Mater.* **2019**, *18*, 1133−1143.
(16) Mahmoudi, M.; Yu, M.; Serpooshan, V.; Wu, J. C.; Langer, R.; Lee, R. T.; Karp, J. M.; Farokhzad, O. C. Multiscale technologies for treatment of ischemic cardiomyopathy. *Nat. Nanotechnol.* **2017**, *12*, 845−855.
(17) Wu, M.; Meng, Q.; Chen, Y.; Zhang, L.; Li, M.; Cai, X.; Li, Y.; Yu, P.; Zhang, L.; Shi, J. Large Pore-Sized Hollow Mesoporous Organosilica for Redox-Responsive Gene Delivery and Synergistic Cancer Chemotherapy. *Adv. Mater.* **2016**, *28*, 1963−1969.
(18) Aizik, G.; Waiskopf, N.; Agbaria, M.; Levi-Kalisman, Y.; Banin, U.; Golomb, G. Delivery of Liposomal Quantum Dots via Monocytes for Imaging of Inflamed Tissue. *ACS Nano* **2017**, *11*, 3038−3051.
(19) Chen, Q.; Espey, M. G.; Krishna, M. C.; Mitchell, J. B.; Corpe, C. P.; Buettner, G. R.; Shacter, E.; Levine, M. Pharmacologic ascorbic acid concentrations selectively kill cancer cells: action as a pro-drug to deliver hydrogen peroxide to tissues. *Proc. Natl. Acad. Sci. U. S. A.* **2005**, *102*, 13604−13609.
(20) Espinosa, A.; Di Corato, R.; Kolosnjaj-Tabi, J.; Flaud, P.; Pellegrino, T.; Wilhelm, C. Duality of Iron Oxide Nanoparticles in Cancer Therapy: Amplification of Heating Efficiency by Magnetic Hyperthermia and Photothermal Bimodal Treatment. *ACS Nano* **2016**, *10*, 2436−2446.
(21) Hanahan, D.; Weinberg, R. A. Hallmarks of cancer: the next generation. *Cell* **2011**, *144*, 646−674.
(22) Bao, L.; Haque, A.; Jackson, K.; Hazari, S.; Moroz, K.; Jetly, R.; Dash, S. Increased expression of P-glycoprotein is associated with doxorubicin chemoresistance in the metastatic 4T1 breast cancer model. *Am. J. Pathol.* **2011**, *178*, 838−852.
(23) Wartenberg, M.; Richter, M.; Datchev, A.; Gunther, S.; Milosevic, N.; Bekhite, M. M.; Figulla, H. R.; Aran, J. M.; Petriz, J.; Sauer, H. Glycolytic pyruvate regulates P-Glycoprotein expression in multicellular tumor spheroids via modulation of the intracellular redox state. *J. Cell. Biochem.* **2010**, *109*, 434−446.
(24) Lunt, S. Y.; Vander Heiden, M. G. Aerobic glycolysis: meeting the metabolic requirements of cell proliferation. *Annu. Rev. Cell Dev. Biol.* **2011**, *27*, 441−464.
(25) Lim, E. K.; Kim, T.; Paik, S.; Haam, S.; Huh, Y. M.; Lee, K. Nanomaterials for theranostics: recent advances and future challenges. *Chem. Rev.* **2015**, *115*, 327−394.
(26) Miao, Q.; Xie, C.; Zhen, X.; Lyu, Y.; Duan, H.; Liu, X.; Jokerst, J. V.; Pu, K. Molecular afterglow imaging with bright, biodegradable polymer nanoparticles. *Nat. Biotechnol.* **2017**, *35*, 1102−1110.
(27) Cheng, P.; Miao, Q.; Li, J.; Huang, J.; Xie, C.; Pu, K. Unimolecular Chemo-fluoro-luminescent Reporter for Crosstalk-Free Duplex Imaging of Hepatotoxicity. *J. Am. Chem. Soc.* **2019**, *141*, 10581−10584.
(28) Untch, M.; Mobus, V.; Kuhn, W.; Muck, B. R.; Thomssen, C.; Bauerfeind, I.; Harbeck, N.; Werner, C.; Lebeau, A.; Schneeweiss, A.; Kahlert, S.; von Koch, F.; Petry, K. U.; Wallwiener, D.; Kreienberg, R.; Albert, U. S.; Luck, H. J.; Hinke, A.; Janicke, F.; Konecny, G. E. Intensive dose-dense compared with conventionally scheduled preoperative chemotherapy for high-risk primary breast cancer. *J. Clin. Oncol.* **2009**, *27*, 2938−2945.
(29) Ye, S.; Rao, J.; Qiu, S.; Zhao, J.; He, H.; Yan, Z.; Yang, T.; Deng, Y.; Ke, H.; Yang, H.; Zhao, Y.; Guo, Z.; Chen, H. Rational Design of Conjugated Photosensitizers with Controllable Photoconversion for Dually Cooperative Phototherapy. *Adv. Mater.* **2018**, *30*, 1801216.
(30) Milane, L.; Ganesh, S.; Shah, S.; Duan, Z. F.; Amiji, M. Multimodal strategies for overcoming tumor drug resistance: hypoxia, the Warburg effect, stem cells, and multifunctional nanotechnology. *J. Controlled Release* **2011**, *155*, 237−247.
(31) Wang, S.; Huang, P.; Chen, X. Hierarchical Targeting Strategy for Enhanced Tumor Tissue Accumulation/Retention and Cellular Internalization. *Adv. Mater.* **2016**, *28*, 7340−7364.
(32) Srinivasarao, M.; Low, P. S. Ligand-Targeted Drug Delivery. *Chem. Rev.* **2017**, *117*, 12133−12164.
(33) Yuan, Y.; Wang, L.; Du, W.; Ding, Z.; Zhang, J.; Han, T.; An, L.; Zhang, H.; Liang, G. Intracellular Self-Assembly of Taxol Nanoparticles for Overcoming Multidrug Resistance. *Angew. Chem., Int. Ed.* **2015**, *54* (33), 9700−4.
(34) Ye, D.; Shuhendler, A. J.; Cui, L.; Tong, L.; Tee, S. S.; Tikhomirov, G.; Felsher, D. W.; Rao, J. Bioorthogonal cyclization-mediated in situ self-assembly of small-molecule probes for imaging caspase activity in vivo. *Nat. Chem.* **2014**, *6*, 519−526.
(35) Zhang, D.; Qi, G. B.; Zhao, Y. X.; Qiao, S. L.; Yang, C.; Wang, H. In Situ Formation of Nanofibers from Purpurin18-Peptide Conjugates and the Assembly Induced Retention Effect in Tumor Sites. *Adv. Mater.* **2015**, *27*, 6125−6130.
(36) Zou, R.; Wang, Q.; Wu, J.; Wu, J.; Schmuck, C.; Tian, H. Peptide self-assembly triggered by metal ions. *Chem. Soc. Rev.* **2015**, *44*, 5200−5219.
(37) Wang, H.; Feng, Z.; Xu, B. Intercellular Instructed-Assembly Mimics Protein Dynamics To Induce Cell Spheroids. *J. Am. Chem. Soc.* **2019**, *141* (18), 7271−7274.
(38) Sharma, A.; Lee, M.-G.; Shi, H.; Won, M.; Arambula, J. F.; Sessler, J. L.; Lee, J. Y.; Chi, S.-G.; Kim, J. S. Overcoming Drug Resistance by Targeting Cancer Bioenergetics with an Activatable Prodrug. *Chem.* **2018**, *4*, 2370−2383.
(39) Qi, G. B.; Gao, Y. J.; Wang, L.; Wang, H. Self-Assembled Peptide-Based Nanomaterials for Biomedical Imaging and Therapy. *Adv. Mater.* **2018**, *30*, 1703444.
(40) Jin, C.; He, J.; Zou, J.; Xuan, W.; Fu, T.; Wang, R.; Tan, W. Phosphorylated lipid-conjugated oligonucleotide selectively anchors on cell membranes with high alkaline phosphatase expression. *Nat. Commun.* **2019**, *10*, 2704.
(41) Yu, Z.; Wang, M.; Pan, W.; Wang, H.; Li, N.; Tang, B. Tumor microenvironment-triggered fabrication of gold nanomachines for tumor-specific photoacoustic imaging and photothermal therapy. *Chem. Sci.* **2017**, *8*, 4896−4903.
(42) Santra, S.; Kaittanis, C.; Santiesteban, O. J.; Perez, J. M. Cell-specific, activatable, and theranostic prodrug for dual-targeted cancer imaging and therapy. *J. Am. Chem. Soc.* **2011**, *133* (41), 16680−16688.
(43) Tang, Z.; Zhang, H.; Liu, Y.; Ni, D.; Zhang, H.; Zhang, J.; Yao, Z.; He, M.; Shi, J.; Bu, W. Antiferromagnetic Pyrite as the Tumor Microenvironment-Mediated Nanoplatform for Self-Enhanced Tumor Imaging and Therapy. *Adv. Mater.* **2017**, *29*, 1701683−1701683.
(44) Ma, T.; Hou, Y.; Zeng, J.; Liu, C.; Zhang, P.; Jing, L.; Shangguan, D.; Gao, M. Dual-Ratiometric Target-Triggered Fluorescent Probe for Simultaneous Quantitative Visualization of Tumor Microenvironment Protease Activity and pH in Vivo. *J. Am. Chem. Soc.* **2018**, *140*, 211−218.
(45) Lin, H.; Chen, Y.; Shi, J. Nanoparticle-triggered in situ catalytic chemical reactions for tumour-specific therapy. *Chem. Soc. Rev.* **2018**, *47*, 1938−1958.
(46) Zheng, X.; Mao, H.; Huo, D.; Wu, W.; Liu, B.; Jiang, X. Successively activatable ultrasensitive probe for imaging tumour acidity and hypoxia. *Nat. Bio. Eng.* **2017**, *1*, 1−9.
(47) Gao, Z.; Hou, Y.; Zeng, J.; Chen, L.; Liu, C.; Yang, W.; Gao, M. Tumor Microenvironment-Triggered Aggregation of Antiphagocytosis (99m) Tc-Labeled Fe3 O4 Nanoprobes for Enhanced Tumor Imaging In Vivo. *Adv. Mater.* **2017**, *29*, 1701095−1701095.
(48) Bailey, K. M.; Wojtkowiak, J. W.; Hashim, A. I.; Gillies, R. J. Targeting the metabolic microenvironment of tumors. *Adv. Pharmacol.* **2012**, *65*, 63−107.
(49) He, S.; Li, J.; Lyu, Y.; Huang, J.; Pu, K. Near-Infrared Fluorescent Macromolecular Reporters for Real-Time Imaging and Urinalysis of Cancer Immunotherapy. *J. Am. Chem. Soc.* **2020**, *142*, 7075−7082.

https://dx.doi.org/10.1021/jacs.0c10755
J. Am. Chem. Soc. 2020, 142, 21502−21512

(50) Lyu, Y.; Zhen, X.; Miao, Y.; Pu, K. Reaction-Based Semiconducting Polymer Nanoprobes for Photoacoustic Imaging of Protein Sulfenic Acids. *ACS Nano* **2017**, *11*, 358−367.
(51) Zheng, Y.; Ji, X.; Yu, B.; Ji, K.; Gallo, D.; Csizmadia, E.; Zhu, M.; Choudhury, M. R.; De La Cruz, L. K. C.; Chittavong, V.; Pan, Z.; Yuan, Z.; Otterbein, L. E.; Wang, B. Enrichment-triggered prodrug activation demonstrated through mitochondria-targeted delivery of doxorubicin and carbon monoxide. *Nat. Chem.* **2018**, *10*, 787−794.
(52) Yuan, Y.; Zhang, J.; Qi, X.; Li, S.; Liu, G.; Siddhanta, S.; Barman, I.; Song, X.; McMahon, M. T.; Bulte, J. W. M. Furin-mediated intracellular self-assembly of olsalazine nanoparticles for enhanced magnetic resonance imaging and tumour therapy. *Nat. Mater.* **2019**, *18*, 1376−1383.
(53) Yang, G.; Xu, L.; Chao, Y.; Xu, J.; Sun, X.; Wu, Y.; Peng, R.; Liu, Z. Hollow MnO2 as a tumor-microenvironment-responsive biodegradable nano-platform for combination therapy favoring antitumor immune responses. *Nat. Commun.* **2017**, *8*, 902.
(54) Liu, J.; Yu, M.; Zhou, C.; Yang, S.; Ning, X.; Zheng, J. Passive tumor targeting of renal-clearable luminescent gold nanoparticles: long tumor retention and fast normal tissue clearance. *J. Am. Chem. Soc.* **2013**, *135*, 4978−4981.
(55) Du, B.; Jiang, X.; Das, A.; Zhou, Q.; Yu, M.; Jin, R.; Zheng, J. Glomerular barrier behaves as an atomically precise bandpass filter in a sub-nanometre regime. *Nat. Nanotechnol.* **2017**, *12*, 1096−1102.
(56) Li, L.; Scheiger, J. M.; Levkin, P. A. Design and Applications of Photoresponsive Hydrogels. *Adv. Mater.* **2019**, *31*, 1807333.
(57) Diekmann, J.; Gontcharov, J.; Frobel, S.; Torres Ziegenbein, C.; Zinth, W.; Gilch, P. The Photoaddition of a Psoralen to DNA Proceeds via the Triplet State. *J. Am. Chem. Soc.* **2019**, *141*, 13643−13653.
(58) Shi, H.; Zhang, C. J.; Chen, G. Y.; Yao, S. Q. Cell-based proteome profiling of potential dasatinib targets by use of affinity-based probes. *J. Am. Chem. Soc.* **2012**, *134*, 3001−3014.
(59) Li, Z.; Hao, P.; Li, L.; Tan, C. Y.; Cheng, X.; Chen, G. Y.; Sze, S. K.; Shen, H. M.; Yao, S. Q. Design and synthesis of minimalist terminal alkyne-containing diazirine photo-crosslinkers and their incorporation into kinase inhibitors for cell- and tissue-based proteome profiling. *Angew. Chem., Int. Ed.* **2013**, *52*, 8551−8556.
(60) Jankovic, B.; Gulzar, A.; Zanobini, C.; Bozovic, O.; Wolf, S.; Stock, G.; Hamm, P. Photocontrolling Protein-Peptide Interactions: From Minimal Perturbation to Complete Unbinding. *J. Am. Chem. Soc.* **2019**, *141*, 10702−10710.
(61) Giess, M.; Munoz-Lopez, A.; Buchmuller, B.; Kubik, G.; Summerer, D. Programmable Protein-DNA Cross-Linking for the Direct Capture and Quantification of 5-Formylcytosine. *J. Am. Chem. Soc.* **2019**, *141*, 9453−9457.
(62) Yao, C.; Tang, H.; Wu, W.; Tang, J.; Guo, W.; Luo, D.; Yang, D. Double Rolling Circle Amplification Generates Physically Cross-Linked DNA Network for Stem Cell Fishing. *J. Am. Chem. Soc.* **2020**, *142*, 3422−3429.
(63) Zhao, T.; Wang, P.; Li, Q.; Al-Khalaf, A. A.; Hozzein, W. N.; Zhang, F.; Li, X.; Zhao, D. Near-Infrared Triggered Decomposition of Nanocapsules with High Tumor Accumulation and Stimuli Responsive Fast Elimination. *Angew. Chem., Int. Ed.* **2018**, *57*, 2611−2615.
(64) Cheng, X.; Sun, R.; Yin, L.; Chai, Z.; Shi, H.; Gao, M. Light-Triggered Assembly of Gold Nanoparticles for Photothermal Therapy and Photoacoustic Imaging of Tumors In Vivo. *Adv. Mater.* **2017**, *29*, 1604894−1604894.
(65) De Laet, N.; Llamas, E. M.; Madder, A. Templated DNA Cross-Linking: Towards a Non-Invasive Singlet-Oxygen-Based Triggering Method. *ChemPhotoChem.* **2018**, *2*, 575−579.
(66) Op de Beeck, M.; Madder, A. Unprecedented C-selective interstrand cross-linking through in situ oxidation of furan-modified oligodeoxynucleotides. *J. Am. Chem. Soc.* **2011**, *133*, 796−807.
(67) Op de Beeck, M.; Madder, A. Sequence specific DNA cross-linking triggered by visible light. *J. Am. Chem. Soc.* **2012**, *134*, 10737−40.
(68) Schmidt, M. J.; Summerer, D. Red-light-controlled protein-RNA crosslinking with a genetically encoded furan. *Angew. Chem., Int. Ed.* **2013**, *52*, 4690−3.
(69) Schmidt, M. J.; Weber, A.; Pott, M.; Welte, W.; Summerer, D. Structural basis of furan-amino acid recognition by a polyspecific aminoacyl-tRNA-synthetase and its genetic encoding in human cells. *ChemBioChem* **2014**, *15*, 1755−1760.
(70) Barbieri, I.; Kouzarides, T. Role of RNA modifications in cancer. *Nat. Rev. Cancer* **2020**, *20*, 303−322.
(71) Sun, L.; Fazal, F. M.; Li, P.; Broughton, J. P.; Lee, B.; Tang, L.; Huang, W.; Kool, E. T.; Chang, H. Y.; Zhang, Q. C. RNA structure maps across mammalian cellular compartments. *Nat. Struct. Mol. Biol.* **2019**, *26*, 322−330.
(72) Costales, M. G.; Haga, C. L.; Velagapudi, S. P.; Childs-Disney, J. L.; Phinney, D. G.; Disney, M. D. Small Molecule Inhibition of microRNA-210 Reprograms an Oncogenic Hypoxic Circuit. *J. Am. Chem. Soc.* **2017**, *139*, 3446−3455.
(73) Piwecka, M.; Glazar, P.; Hernandez-Miranda, L. R.; Memczak, S.; Wolf, S. A.; Rybak-Wolf, A.; Filipchyk, A.; Klironomos, F.; Cerda Jara, C. A.; Fenske, P.; Trimbuch, T.; Zywitza, V.; Plass, M.; Schreyer, L.; Ayoub, S.; Kocks, C.; Kuhn, R.; Rosenmund, C.; Birchmeier, C.; Rajewsky, N. Loss of a mammalian circular RNA locus causes miRNA deregulation and affects brain function. *Science* **2017**, *357*, 6357.
(74) Warner, K. D.; Hajdin, C. E.; Weeks, K. M. Principles for targeting RNA with drug-like small molecules. *Nat. Rev. Drug Discovery* **2018**, *17*, 547−558.
(75) Haniff, H. S.; Knerr, L.; Liu, X.; Crynen, G.; Bostrom, J.; Abegg, D.; Adibekian, A.; Lekah, E.; Wang, K. W.; Cameron, M. D.; Yildirim, I.; Lemurell, M.; Disney, M. D. Design of a small molecule that stimulates vascular endothelial growth factor A enabled by screening RNA fold-small molecule interactions. *Nat. Chem.* **2020**, *12*, 952−961.
(76) Gao, Y.; Sun, R.; Zhao, M.; Ding, J.; Wang, A.; Ye, S.; Zhang, Y.; Mao, Q.; Xie, W.; Ma, G.; Shi, H. Sulfenic Acid-Mediated on-Site-Specific Immobilization of Mitochondrial-Targeted NIR Fluorescent Probe for Prolonged Tumor Imaging. *Anal. Chem.* **2020**, *92*, 6977−6983.
(77) Markova, L. I.; Malinovskii, V. L.; Patsenker, L. D.; Haner, R. J-vs. H-type assembly: pentamethine cyanine (Cy5) as a near-IR chiroptical reporter. *Chem. Commun.* **2013**, *49*, 5298−5300.
(78) Schroder, M.; Kaufman, R. J. The mammalian unfolded protein response. *Annu. Rev. Biochem.* **2005**, *74*, 739−789.

https://dx.doi.org/10.1021/jacs.0c10755
J. Am. Chem. Soc. 2020, 142, 21502−21512